

Title	Solution processed ZnO homogeneous quasisuperlattice materials
Authors	Buckley, Darragh; McNulty, David; Zubialeovich, Vitaly Z.; Parbrook, Peter J.; O'Dwyer, Colm
Publication date	2017-11
Original Citation	Buckley, D., McNulty, D., Zubialeovich, V., Parbrook, P. and O'Dwyer, C. (2017) 'Solution processed ZnO homogeneous quasisuperlattice materials', Journal of Vacuum Science & Technology A: Vacuum, Surfaces, and Films, 35(6), 061517 (11pp). doi: 10.1116/1.5001758
Type of publication	Article (peer-reviewed)
Link to publisher's version	<a href="http://avs.scitation.org/doi/10.1116/1.5001758">http://avs.scitation.org/doi/10.1116/1.5001758</a> - 10.1116/1.5001758
Rights	© 2017, AIP Publishing. Published by the AVS. This article may be downloaded for personal use only. Any other use requires prior permission of the author and AIP Publishing. The following article appeared in Journal of Vacuum Science & Technology A: Vacuum, Surfaces and Films, Vol 35, 061517 (2017) and may be found at <a href="http://avs.scitation.org/doi/abs/10.1116/1.5001758">http://avs.scitation.org/doi/abs/10.1116/1.5001758</a>
Download date	2024-09-21 06:32:29
Item downloaded from	<a href="https://hdl.handle.net/10468/5242">https://hdl.handle.net/10468/5242</a>



# UCC

**University College Cork, Ireland**  
Coláiste na hOllscoile Corcaigh

## Solution processed ZnO homogeneous quasisuperlattice materials

Darragh Buckley, David McNulty, Vitaly Zubialevich, Peter Parbrook, and Colm O'Dwyer

Citation: *Journal of Vacuum Science & Technology A: Vacuum, Surfaces, and Films* **35**, 061517 (2017);

View online: <https://doi.org/10.1116/1.5001758>

View Table of Contents: <http://avs.scitation.org/toc/jva/35/6>

Published by the [American Vacuum Society](#)

---

### Articles you may be interested in

[Variation of index of refraction in cobalt doped ZnO nanostructures](#)  
*Journal of Applied Physics* **122**, 165304 (2017); 10.1063/1.5001713

[Rhenium-doped MoS<sub>2</sub> films](#)  
*Applied Physics Letters* **111**, 203101 (2017); 10.1063/1.4995220

[Minority carrier diffusion length for electrons in an extended SWIR InAs/AlSb type-II superlattice photodiode](#)  
*Applied Physics Letters* **111**, 201106 (2017); 10.1063/1.5005097

[A broadband antireflective nanostructure with Ag nanoparticles on SiO<sub>2</sub> nanocolumns](#)  
*Applied Physics Letters* **111**, 201602 (2017); 10.1063/1.5000327

[Effects of Ni d-levels on the electronic band structure of Ni<sub>x</sub>Cd<sub>1-x</sub>O semiconducting alloys](#)  
*Journal of Applied Physics* **122**, 185703 (2017); 10.1063/1.4986967

[Coevaporation and structuring of titanium–aluminum alloy thin films](#)  
*Journal of Vacuum Science & Technology A: Vacuum, Surfaces, and Films* **35**, 061603 (2017);  
10.1116/1.4999565

---



## Instruments for Advanced Science

Contact Hiden Analytical for further details:

[www.HidenAnalytical.com](http://www.HidenAnalytical.com)

[info@hiden.co.uk](mailto:info@hiden.co.uk)

[CLICK TO VIEW](#) our product catalogue



#### Gas Analysis

- › dynamic measurement of reaction gas streams
- › catalysis and thermal analysis
- › molecular beam studies
- › dissolved species probes
- › fermentation, environmental and ecological studies



#### Surface Science

- › UHV TPD
- › SIMS
- › end point detection in ion beam etch
- › elemental imaging - surface mapping



#### Plasma Diagnostics

- › plasma source characterization
- › etch and deposition process reaction
- › kinetic studies
- › analysis of neutral and radical species



#### Vacuum Analysis

- › partial pressure measurement and control of process gases
- › reactive sputter process control
- › vacuum diagnostics
- › vacuum coating process monitoring

# Solution processed ZnO homogeneous quasisuperlattice materials

Darragh Buckley and David McNulty

School of Chemistry, University College Cork, Cork T12 YN60, Ireland

Vitaly Zubialevich

Tyndall National Institute, Lee Maltings, Cork T12 R5CP, Ireland

Peter Parbrook

Tyndall National Institute, Lee Maltings, Cork T12 R5CP, Ireland and Department of Electrical and Electronic Engineering, University College Cork, Cork T12 YN60, Ireland

Colm O'Dwyer<sup>a)</sup>

School of Chemistry, University College Cork, Cork T12 YN60, Ireland and Tyndall National Institute, Lee Maltings, Cork T12 R5CP, Ireland

(Received 26 August 2017; accepted 26 October 2017; published 17 November 2017)

Heterogeneous multilayered oxide channel materials have enabled low temperature, high mobility thin film transistor technology by solution processing. The authors report the growth and characterization of solution-based, highly uniform and c-axis orientated zinc oxide (ZnO) single and multilayered thin films. Quasisuperlattice (QSL) metal oxide thin films are deposited by spin-coating and the structural, morphological, optical, electronic, and crystallographic properties are investigated. In this work, the authors show that uniform, coherent multilayers of ZnO can be produced from liquid precursors using an iterative coating-drying technique that shows epitaxial-like growth on SiO<sub>2</sub>, at a maximum temperature of 300 °C in air. As QSL films are grown with a greater number of constituent layers, the crystal growth direction changes from m-plane to c-plane, confirmed by x-ray and electron diffraction. The film surface is smooth for all QSLs with root mean square roughness <0.14 nm. X-ray photoelectron spectroscopy (XPS) and photoluminescence (PL) of electronic defects in the QSL structure show a dependence of defect emission on the QSL thickness, and PL mapping demonstrates that the defect signature is consistent across the QSL film in each case. XPS and valence-band analysis shown a remarkably consistent surface composition and electronic structure during the annealing process developed here. *Published by the AVS.*

<https://doi.org/10.1116/1.5001758>

## I. INTRODUCTION

Thin-film transistors (TFTs) are the fundamental building blocks for macroelectronics.<sup>1</sup> TFTs are used in a broad range of devices such as sensing devices and digital x-ray imaging but have their largest application in display technology.<sup>2,3</sup> High field-effect mobility TFT devices can be made from low-temperature processed polysilicon; however, these suffer from high fabrication cost and nonuniformity, and typically require specific substrate types, high temperatures, and vacuum deposition atmospheres. Organic semiconductors have also been investigated as a cheaper, more flexible alternative yet present very low field-effect mobility in comparison to silicon-based devices.<sup>4</sup> For use in TFT technology, a highly stable, high mobility, controllably thin, uniform and transparent metal oxide is required.<sup>5</sup> Among the TFTs, zinc oxide (ZnO)-based materials are attractive for use in flexible displays because of their higher mobility and lower processing temperature than conventional hydrogenated amorphous Si (a-Si:H) TFTs.<sup>6</sup> ZnO TFTs have been fabricated on flexible substrates and are suited to this due to their lower processing temperature.<sup>7</sup>

ZnO has attracted the initial interest in optoelectronics<sup>8–18</sup> due to its direct wide bandgap ( $E_g \sim 3.3$  eV at 300 K),<sup>19</sup> and a

conductivity influenced by defects and cation/anion vacancies, its ability to alloy with other metal in oxide form, and a lattice that facilitates interstitial doping.<sup>19</sup> ZnO is reported as being the best binary compound for oxide TFT application;<sup>20</sup> however, the electronic properties of ZnO can be improved with the addition of an n-type dopant. Group-III elements such as Al, Ga, and In can be added as electron donors to the conduction band (CB), increasing electron concentration and TFT performance.<sup>19</sup> ZnO is also an attractive material as it can be prepared by several techniques including spray pyrolysis,<sup>21</sup> pulsed laser deposition,<sup>22</sup> rf sputtering,<sup>23</sup> chemical vapor deposition,<sup>24</sup> and solution processed methods.<sup>25</sup> Solution processing offers a method of coating a wide range of substrate shapes to enable new applications as channel materials in flexible, wearable, and plastic electronics.<sup>26</sup> Solution processed deposition techniques employ liquid-based precursors to create films and nanostructures by spin-coating,<sup>27</sup> dip-coating,<sup>28</sup> ink-jet printing, and gravure printing.<sup>29</sup> Liquid precursor solutions can be alkoxides, nitrates, and carboxylates,<sup>30</sup> or other more complex inorganic-organic species. Ideally, they should be stable in storage (nonvolatile), but still allow efficient chemical conversion to oxide form upon heating, hydrolysis, photolysis, or by other means.<sup>31</sup> Using these techniques, solution processed undoped ZnO TFTs have been produced with carrier mobilities as high as  $1.6 \text{ cm}^2 \text{ V}^{-1} \text{ s}^{-1}$  (Ref. 32) or at temperatures as low as 250 °C.<sup>33</sup> The demand

<sup>a)</sup> Author to whom correspondence should be addressed; electronic mail: c.odwyer@ucc.ie

for materials that are low cost and high performance drives research into transparent conductive oxides and amorphous oxide thin films, leading to a range of crystalline and amorphous oxides for TFTs including indium-gallium-zinc oxide (IGZO), indium zinc oxide (IZO), zinc-tin oxide, aluminum zinc oxide, hafnium-zinc-tin oxide, and others.<sup>1,20,34–36</sup>

Transparency in the visible is advantageous for some applications, particularly for “invisible electronic circuits” in future of display technology and electronics, with the proviso that lower-temperature processing and control of conduction/mobility is improved.<sup>37</sup> However, good control over solution-processing is paramount for high quality electronic material grade ZnO and its alloyed or doped counterparts, particularly when grown at a low temperature. At just above the decomposition temperatures for the organic moieties of Zn-based precursors, effective removal of these species is critical for crystallization and defined stoichiometry. It is also imperative that high crystal quality epitaxial-like thin films can be formed from solution processing to compete with physical deposition methods. Oxygen vacancy formation within ZnO can sometimes be balanced at higher temperatures in O<sub>2</sub> atmospheres, where oxidation annihilates oxygen vacancy density, but it has yet to be determined if surface ionic vacancy formation is modified during lower temperature crystallization to a high electronic quality thin film.<sup>35</sup> Other interstitial and vacancy defects are also formed in ZnO and understanding the nature of these during crystallization of thin films at lower temperatures remains a challenge since stoichiometry and composition determine conductivity and free carrier mobility.<sup>38</sup>

Heterostructures involving quasisuperlattice (QSL) of various oxides have demonstrated the formation of structures with spatially varying conduction band characteristics<sup>39</sup> and that carrier mobility can be enhanced at such interfaces,<sup>40</sup> removing dependence on limited Hall mobility in the either of the bulk materials. At oxide interfaces with the dielectric, or between homo- or heterophase interface in quasi or ordered superlattices, trapped charges in an oxide layer or interface from electric field-induced removal of majority carriers that leave a net positive charge density on the surface or interface. These interfaces removed the dependence on bulk carrier mobility of each single semiconductor layer—the interfacial carrier mobility was higher. In<sub>2</sub>O<sub>3</sub>-Ga<sub>2</sub>O<sub>3</sub>-ZnO-Ga<sub>2</sub>O<sub>3</sub>-In<sub>2</sub>O<sub>3</sub> have been reported,<sup>40</sup> with an electronic carrier mobility of  $\mu_e > 40 \text{ cm}^2 \text{ V}^{-1} \text{ s}^{-1}$ . A 2DEG formed at the interface has also been reported using ZnO/ZnMgO (Ref. 41) interfaces and bilayered In<sub>2</sub>O<sub>3</sub>-ZnO TFTs processed from solution can now achieve over  $45 \text{ cm}^2 \text{ V}^{-1} \text{ s}^{-1}$  mobility.<sup>42</sup> These trap sites often cause shifts in threshold voltage and affect leakage characteristics. Although some quasisuperlattice structures of heterophases provide higher mobility at the interface compared to the corresponding bulk material layer, homogeneous QSL structures have received limited attention. Such structures may provide controllable thickness and interfacial transport characteristics, but also a consistent refractive index and transparency compared to hetero-QSL structures. A widening of the optical bandgap of similarly grown ZnO thin films with

reducing film thickness has been reported and shows strong evidence toward existence of quantized energy states in solution processed ZnO layers.<sup>43</sup>

This work details the solution processing of ZnO thin films and QSL films on dielectric SiO<sub>2</sub> formed by iterative spin-coating and annealing protocols. We demonstrate that crystalline, epitaxial-like and highly ordered growth of ZnO thin films can be achieved from a precursor liquid at relatively low temperature (max. 300 °C) in air, by a process that uses iterative heating/annealing steps for each layer. We examine the detailed microstructure and growth mechanism of QSL ZnO and the formation of periodic bilayered porous-dense layers that grow with increasing degree of homoepitaxy (c-plane orientation). The composition, structural, and electronic nature of solution processed thin films of ZnO at lower temperature are also determined, and we demonstrate that internal substructure and interfaces provide defect sites that control sub-band photoluminescence (PL) emission, yet XPS proves conclusively that the top surface composition is identical regardless of the number of periods in the QSL. The synthesized films were smooth, stoichiometric ZnO with controllable thickness dependent on the number of layers. Optical characterization of the thin films investigated transmittance of ZnO QSLs on transparent substrates and the optical bandgap, determined from UV/vis spectroscopy. Reflectance spectroscopy confirms, and from work we have previously shown,<sup>44</sup> that QSLs behave as continuous, coherent, dispersive thin films.

## II. EXPERIMENT

### A. Spin coating of ZnO thin films

Zinc oxide thin films were synthesized from zinc acetate dihydrate [Zn(CH<sub>3</sub>COO)<sub>2</sub>·2H<sub>2</sub>O]. The acetate powder was dissolved in 2-methoxyethanol [CH<sub>3</sub>OCH<sub>2</sub>CH<sub>2</sub>OH] to make a 0.75 M solution. An equimolar solution of monoethanolamine was added to the zinc precursor as a stabilizing agent. All chemicals were purchased from Sigma Aldrich. The precursor was heated at 60 °C for 2 h and stirred until a clear, colorless solution is obtained.

Controllably thin and smooth films were prepared by a spin-coating technique. Using a SCS G3 desktop spin coater, ZnO precursor solution was added dropwise to cover substrates and were spun at 3000 rpm for 30 s, including a 5 s ramp time. This process formed a uniform film coating on the cleaned substrates. Thin films were deposited on doped p-type silicon substrates that were covered with an 85 or 300 nm thick layer of thermally grown SiO<sub>2</sub>. Substrates for spin coated samples were cut into square coupons of nominal dimension 1 × 1 cm to ensure even coverage as the samples are rotated about a perpendicular symmetric axis. An acetone, isopropyl alcohol, and deionized water wash combined with sonication was used to ensure that the surface of the wafers were clean of surface contaminants prior to thin film deposition. A UV-Ozone treatment was performed for 30 min using a Novascan UV ozone system to further remove any organic contaminants from the surface. The surface wettability of the thin films to the substrates can be affected by the UV-Ozone

cleaning directly after exposure; to ensure identical deposition conditions, substrates were coated within 1 h of UV-Ozone treatment. After a layer of precursor was spin coated, samples were dried in an open-air convection oven at temperatures between 250 and 270 °C for 5 min. Another layer of liquid precursor was then spun onto the surface followed by more oven-drying. This process was then repeated to acquire the desired film thickness, and the samples were subsequently annealed at 300 °C for 1 h as a final heat treatment.

## B. Surface morphology analysis

Surface morphology of prepared thin films was investigated using atomic force microscopy (AFM) using a Park XE-100 system in the noncontact mode with model SSS\_NCHR enhanced resolution high aspect ratio tips. The XY and Z resolutions of the AFM stepper motor drives are  $\sim 2$  and  $\sim 0.05$  nm, respectively. From AFM data, the root mean square (rms) roughness of the ZnO film surfaces was determined after each successive spin coating until the final thickness. AFM measurements were also used to determine film thickness. Samples were scribed through the center using a scalpel or razor blade, ensuring a thin cut directly down to the SiO<sub>2</sub>. Several measurements are made by AFM at the interface of these cuts to give a consistent depth measurement and this was also carried out after each added coating/layer.

## C. Electron microscopy, electron and x-ray diffraction analysis

Surface and cross-sectional imaging, morphology, and thickness measurements were also conducted by scanning electron microscopy (SEM) using an FEI Quanta 650 FEG high resolution SEM at accelerating voltage in the range of 8–20 kV. Transmission electron microscopy (TEM) was also conducted on lamellar cross-section of the ZnO thin films on SiO<sub>2</sub>/Si. Cross-sectioning of the Si electrodes was carried out with an FEI Helios Nanolab Dual Beam FIB System. Protective layers of carbon and platinum support straps were deposited on the sample surface to minimize surface damage during thinning of the lamella to electron transparency. Cross-sectional TEM sample preparation was performed on slices using a standard FIB lift-out technique. TEM analysis and electron diffraction was conducted using a JEOL JEM-2100 TEM operating at 200 kV. X-ray diffraction (XRD) was used to characterize the crystallographic structure of the ZnO films after each iterative spin coating. XRD analysis of ZnO films was performed using a Philips X'Pert PW3719 diffractometer using Cu K $\alpha$  radiation (40 kV and 35 mA) scanned between 10° and 80° ( $2\theta$ ).

## D. X-ray photoelectron and photoluminescence spectroscopy

The chemical bonding state of the top surface, the effective conductivity type and valence band (VB) spectra were determined by x-ray photoelectron spectroscopy, using a Kratos Axis 165 equipped with a monochromatic Al source (K $\alpha$  = 1486.58 eV) with a spot size of 1 mm. The source power was 150 W, the take-off angle was set normal to the sample

surface, the construction and peak fittings in the narrow region core-level spectra were performed using a Shirley type background. Adventitious carbon was used for the charge reference (C 1s) for each measurement. PL spectroscopy was used to probe the electronic structure of the spin coated ZnO thin films. Band-edge and sub-band PL emission was carried out at room temperature using a 325 nm He–Cd laser excitation source with power density of 2 W/cm<sup>2</sup>. PL spectra were recorded using a Horiba iHR320 spectrometer equipped with a thermoelectrically cooled Synapse CCD matrix.

## E. Optical reflectance and transmission spectroscopy

Optical characterization of thin films was conducted using a cage-mounted optical reflectance spectroscopy setup. The reflectivity was obtained at an incident angle of 45° using high precision 360° rotation mount and collection arm with constant path length. Samples were illuminated with a white tungsten halogen lamp collimated to a beam diameter of  $\sim 1$ –2 mm using optical fiber with an output spectral range from 360 to 2400 nm. The reflected light was collected using focusing optics into an Oceanoptics USB2000+ spectrometer (400–1000 nm range) which has an optical resolution of 1.5 nm. To measure the optical transparency of the samples in the 200–1000 nm range, a Thermo Scientific Evolution 60S UV-Visible spectrophotometer with resolution of  $\pm 0.8$  nm illuminated with a xenon light source was used with a custom sample holder. Analysis of transparency data using Tauc plots allowed the calculation of the effective optical bandgap ( $E_g$ ) of the QSLs.

## III. RESULTS AND DISCUSSION

### A. ZnO quasisuperlattice growth

ZnO films and QSL thin films were spin-coated from solution-based precursors directly onto oxidized Si substrates and annealed following the protocol summarized in Fig. 1(a) and outlined in Sec. II. TEM analysis of the cross-sectional structure and morphology of FIB-thinned lamella from single and QSL thin films containing 1, 5, 10, and 20 layers is shown in Figs. 1(b)–1(e). Figure 1(b) confirms that the single layer thin film forms a uniform coating  $\sim 32$ –38 nm thickness on SiO<sub>2</sub> and is consistently the thickest of all QSLs. Subsequent iterative solution processing of ZnO layers results in a periodic QSL structure. Figures 1(f) and 1(g) display the periodic bilayered structure of the 20 layer QSL thin film. Each additional layer in this periodic QSL structure consists of two composite parts: a semiporous ZnO midlayer and a denser ZnO capping layer to form a bilayered structure that defines each layer in the QSL. Banger *et al.* demonstrated a similar layered structure via spin-coating of IZO films and drying in an N<sub>2</sub> atmosphere.<sup>36</sup> This process yielded crystalline films that possessed an inherent layered composition yet do not show the obvious bilayer structure seen from ZnO films in Fig. 1. This dense capping layer is formed during the  $\sim 5$  min drying time of each of the layers between depositions whereas the midlayer and capping layer are crystallized during the postdeposition 1 h anneal at 300 °C.

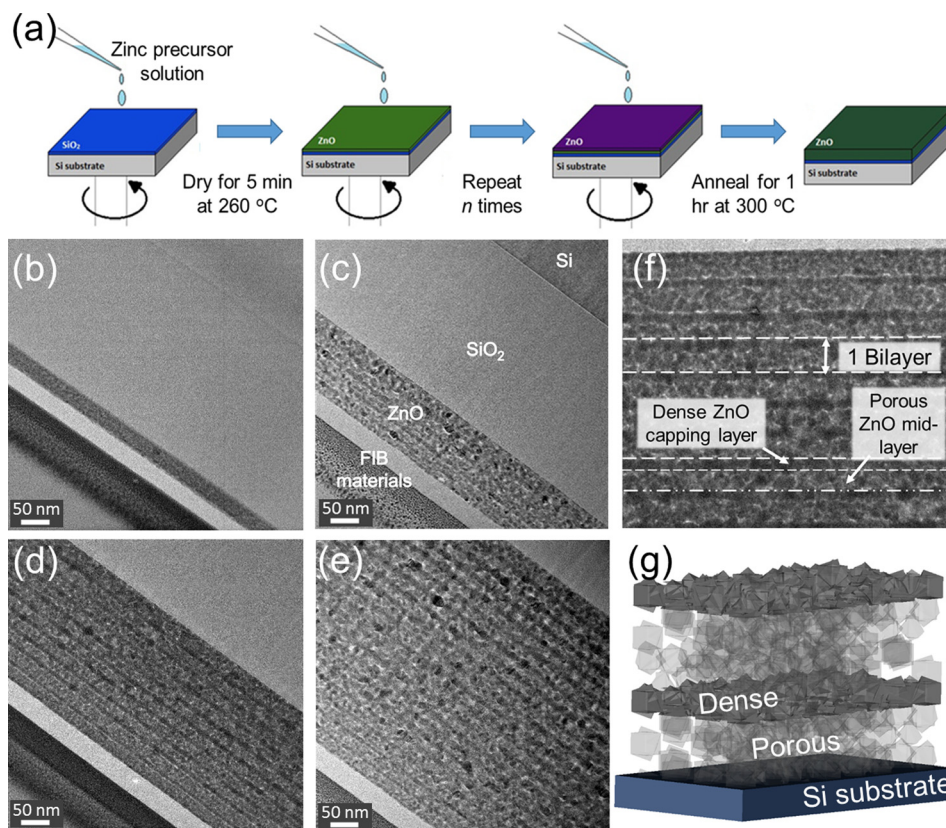


FIG. 1. (Color online) (a) Deposition schematic for spin-coated ZnO thin films. TEM cross-sectional images of (b) 1 layer, (c) 5 layer, (d) 10 layer, and (e) 20 layer ZnO thin films. (f) Profile view of the 10 layer QSL of spin-coated ZnO thin film. (g) Schematic of the bi-layer structure of ZnO films, composing iterative porous layers capped by dense layers.

Both parts of each periodic layer are crystalline, with defined pseudoepitaxial growth. The QSL approach avoids the need for a buffer seed layer to prevent amorphous ZnO growth on SiO<sub>2</sub> that suppresses electronic conductivity, and the initial layer is predominantly m-plane oriented, acting as a template for subsequent growth from iterative spin-coating. X-ray diffraction patterns of single layer and multilayer QSL ZnO thin films show just two major reflections. As seen in Fig. 2(a),

there is a distinct change in the crystalline texture of the QSL films with additional periodic layers. The single spin-coated layer of ZnO shows crystalline growth strictly in the [10 $\bar{1}$ 0] m-plane direction with no other  $[hki]$  reflections present. Further deposition of material and annealing to build-up the homogenous ZnO periodic QSL displays a clear change in crystal growth preference to the [0002] nonpolar c-plane. With five layers in the QSL, nonpolar c-plane diffraction is

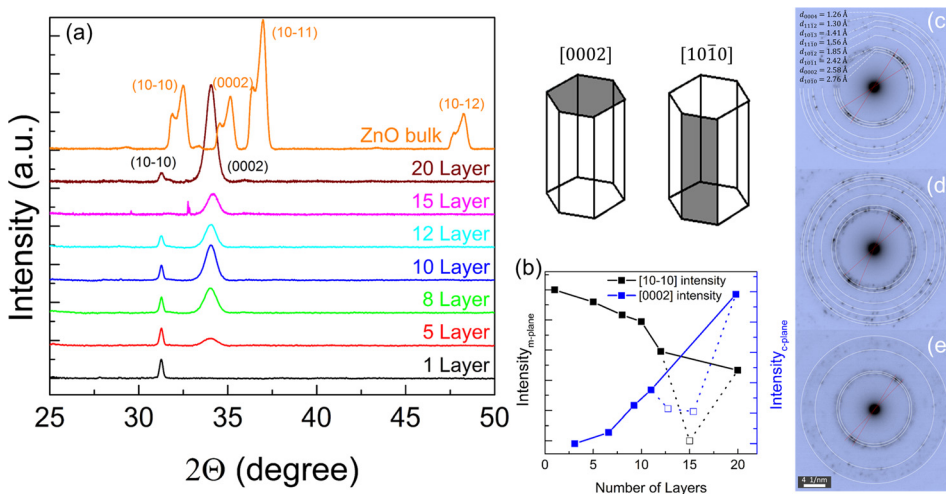


FIG. 2. (Color online) (a) X-ray diffraction patterns for 1–20 layer QSL ZnO thin films with the reference diffraction pattern for bulk ZnO. (b) X-ray reflection intensity of m-plane and c-plane reflections for single and QSL ZnO from (a) highlighting the transition in monocrystalline texture with increased number of layers in the ZnO QSL. (c)–(e) Electron diffraction patterns for 5, 10 and 20 QSL thin films, respectively, showing the represented d-spacings.

noted and in this case, and as observed by TEM in Fig. 1, this corresponds to the dense top layer of ZnO bilayer after each sequential spin coating. The normalized intensity and line-shape of the m-plane reflections remain relatively unchanged ( $2\theta = 31.27^\circ$  irrespective of cumulative annealing) and the porous portion of each layer corresponds to a similar type of thin film formed after the single layer coating. As the volume fraction of dense ZnO increases with the number of coatings, so does the intensity of the nonpolar c-plane reflections [Fig. 2(b)]. As will be shown later, this results from a greater cumulative annealing energy, facilitating the layer-on-layer homoeptaxy. The intensity of the [0002] reflection increases with continual deposition, displaying an epitaxial-like growth. With repetitive depositions, the film becomes uniformly c-axis orientated due to the formation of further homo-interfaces. The c-plane reflection remains consistently at  $2\theta = 34.08^\circ$ , lower than  $34.4^\circ$  for bulk ZnO (JCPDS #5-664) and is characteristic of nanocrystalline grain content in the QSL film. Furthermore, the absence of peak shifts indicates negligible growth-induced strain in or between high ordered layers in the QSL structure.<sup>38</sup>

Electron diffraction (ED) patterns for 5, 10, and 20 layer QSL ZnO thin films are shown in Figs. 2(c)–2(e). An electron diffraction pattern for the one layer ZnO could not be collected due to the small spot size presented by such a thin (<40 nm thick) cross-section. In Figs. 2(c)–2(e), we note the intensity of the closely spaced [10 $\bar{1}$ 0] and [0002] matches very closely with relative intensity changes in XRD patterns; c-plane intensity dominates for greater QSL thickness. The observation of rings in the ED patterns indicates the presence of randomly orientated nanocrystalline grains within the less-dense portion of each bilayer in the QSL, and the rings acquire a quasi-hexagonal pattern at 20 layers thickness [Fig. 2(e)]. Higher order peaks are found in the electron diffraction pattern for the ZnO films that are not evidenced in the XRD data, primarily because of the localized beam area of selected area electron diffraction, which samples statistically fewer of the various orientations of the nanocrystalline region compared to XRD of the entire film. These rings shown in Fig. 2(c) highlight the presence of the [10 $\bar{1}$ 1], [10 $\bar{1}$ 2], [11 $\bar{1}$ 0], [10 $\bar{1}$ 3], [11 $\bar{1}$ 2], and [0004] reflections; however, these have a very low relative intensity with respect to the [10 $\bar{1}$ 0] and [0002] reflections, which are present in the XRD patterns. Furthermore, there is a narrowing in the c-plane reflection from Figs. 2(c)–2(e) that coincides with the greater intensity of the [0002] and iso-axial orientation of the nanocrystalline substructure with increasing QSL layer deposition seen from XRD reflections.

## B. Thickness control in solution processed QSL ZnO

In Fig. 3(a), we measured the thickness of both dense and less dense portions of each periodic bilayer in the QSL by TEM of FIB-sectional electron transparent lamella, as a function of the total number of iterative depositions. As shown earlier, the initial m-plane oriented single layer is  $\sim 38$  nm in thickness, and is consistent for all QSL irrespective of the number of subsequent depositions. We note that this

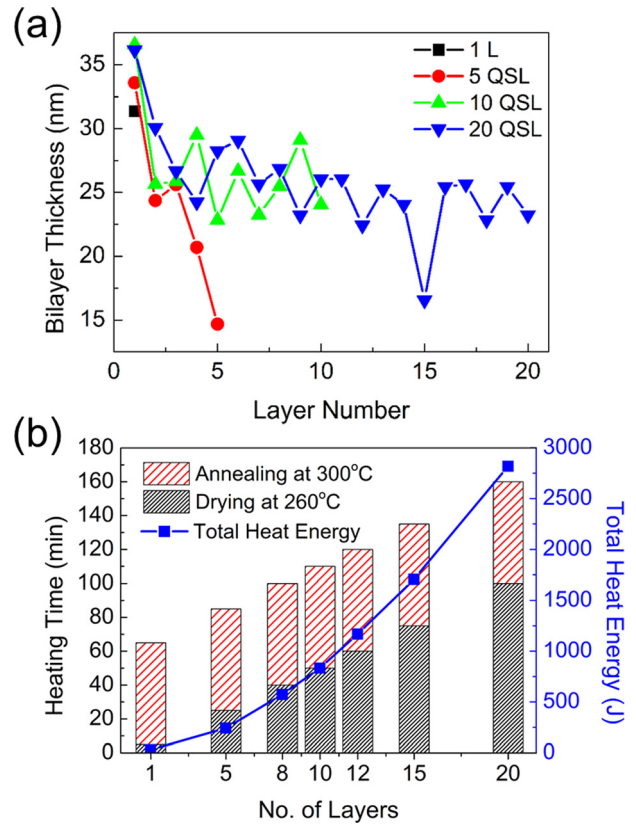


Fig. 3. (Color online) (a) Line profile thickness measurements from individual cross-sectional TEM data of single and QSL ZnO films. (b) Heating profile of each thin film sample based on drying and annealing time in comparison to total heat energy transferred to the system in this process.

initial film recrystallizes to c-plane orientation as the number of layers (and annealing energy) is increased, but thickness remains largely unchanged. Characteristically, the second to fourth bilayers are slightly thinner than the initial layer, and in QSL with five deposited films, each successive bilayer is thinner. However, for greater QSL number, the thickness tapers to a consistent 22–26 nm thickness. Consistently, the periodic thickness is found in samples where sufficient annealing has caused a dominant change on film orientation to c-plane pseudoepitaxy layer-on-layer.

Figure 3(b) shows the heating profile applied to each QSL sample, dependent on the number of deposited layers. This also displays the heat energy contributed to the sample system by the drying and subsequent annealing process. We calculated the heat energy by using the relation

$$Q = mC_p\Delta T. \quad (1)$$

$\Delta T$  is the correspondent temperature change of the drying and annealing stages, separately. We should state that annealing is within an oven, with air access but an equilibrated surrounding temperature, and so heat loss to the surroundings near the sample was assumed negligible in the calculation. Therefore, this is expanded by including the temperature shifts for both the drying step and final annealing processes. The drying process temperature change is defined as  $\Delta T_A$  and the annealing process is defined as  $\Delta T_B$ .  $C_p = 41.086$  J mol $^{-1}$  K $^{-1}$  is the specific heat capacity of ZnO, and  $m$  is the

mass of the film. The heat energy contributed to a one layer film can therefore be calculated as follows:

$$Q_1 = m_1 C_p \Delta T_A + m_1 C_p \Delta T_B. \quad (2)$$

For multilayer QSLs, however, the drying stage is cumulative, with the increasingly more massive deposits receiving a 260 °C heat treatment after each spin-coat. Therefore,  $C_p \Delta T_A$  must be applied to a sum of all the individual masses that make up the QSL while the final annealing process  $C_p \Delta T_B$  is only applied to the final mass of the film, e.g., for a five layer QSL

$$Q_5 = (m_1 + m_2 + m_3 + m_4 + m_5) C_p \Delta T_A + m_5 C_p \Delta T_B. \quad (3)$$

This can then be generalized to the following equation for application to any film of  $n$  deposited layers:

$$Q_n = C_p \left( \Delta T_A \sum_1^n m_n + \Delta T_B m_n \right). \quad (4)$$

The mass of each layer is calculated by multiplying the thickness of the layer, determined from TEM analysis, by the substrate area to determine the layer volume and subsequently multiplying the volume by the density of ZnO, 5.61 g/cm<sup>3</sup>.

From Fig. 3(b), it is clear the consistent drying stage, which corresponds to the dense capping ZnO portion of each layer in the QSL, contributes to a greater cumulative portion of the total annealing heat energy as the number of layers increases. The formation of the dense capping layer and the porous nanocrystalline content beneath the capping layer, believed to contribute to the variety of electronic defects between samples (*vide infra*), are also dependent on this crucial drying stage in the deposition. Akazawa<sup>38</sup> and Dong *et al.*<sup>45</sup> stated that for ZnO, without a QSL substructure, that increasing the thickness of crystalline ZnO films improves the conductivity once films are sufficiently thick to have a pronounced effect on lattice disorder and relieve stresses that can act as charge carrier trap states. Yamada *et al.* also show a decrease in ZnO resistivity with an increase in film thickness.<sup>46</sup> Crystallinity and c-axis orientation improves as the

film thickness increases in our case and the QSL approach provides a homogenous composition and effective refractive index and surface composition, while also avoiding the amorphous-to-crystalline interface region that is detrimental to conductivity in thinner films.<sup>47</sup>

We analyzed the growth of single and QSL solution processed film in detail using AFM and cross-sectional TEM, shown in Fig. 4(a). The surface topography of ZnO films as a function of number of deposited layers, i.e., thickness, was investigated using AFM. Figures 4(b) and S1 in the supplementary material,<sup>59</sup> shows a representative surface topography of the top surface postannealing. The smooth film surface does not show obvious surface defects, pinholes, or obvious grain boundaries. The corresponding surface rms roughness of a 3 × 3 μm area [Fig. 4(a)] is consistently <0.14 nm forming a thin film QSL set of various thicknesses, confirmation that spin-coating from a liquid precursor can produce uniform and smooth film surfaces, since iterative coating for QSL growth occurs on the dense, smooth upper ZnO surface from the preceding deposition step.

The scribe method with AFM was used to estimate the height difference between the sample surface and the substrate, and provided consistent thickness measurements that were comparable to more accurate method of localized nanoscale thickness measurement employed in TEM cross-sectional imaging. Figure 4(c) shows the line profile of a cleaved ZnO thin film, displaying the substrate surface and the film surface. The height between these two surfaces is then measured as the thickness of the thin film. Thickness values from AFM and TEM show good agreement initially with a deviation after eight coatings of the QSL that diverges as the thickness of the film above eight layers prevents accurate depth measurement by AFM. A near linear relationship between thickness and number of deposited precursor layers was demonstrated in Fig. 4(a). The predicted linear thickness is calculated by multiplying the integer number of layers by the thickness of a one-layer ZnO film, which is m-plane oriented with a thickness of 32–28 nm typically. The divergence of the resulting measurements from this trend indicates that the initially deposited layer is thicker than subsequent layers.

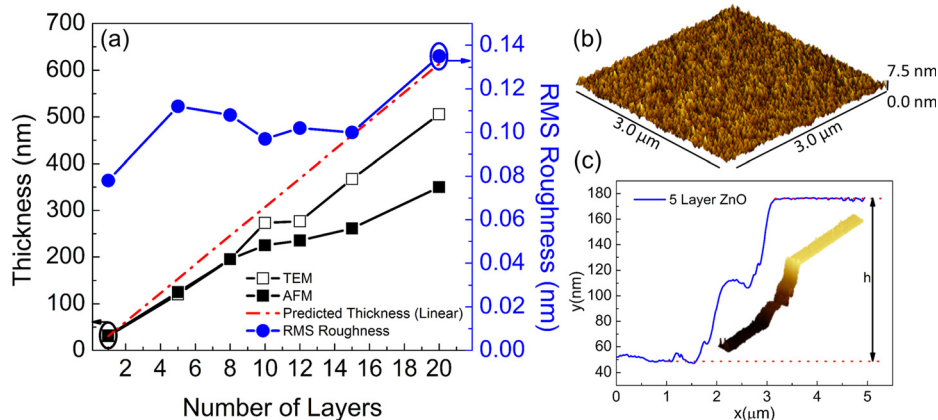


Fig. 4. (Color online) (a) Thickness of ZnO samples with respect to number of deposited layers measured via TEM and AFM, also used to determine the root mean square roughness of the thin film surfaces. (b) 3D AFM surface topography image of ZnO thin film sample. (c) Line profile measurement taken using AFM to determine sample thickness.

### C. ZnO QSL surface composition and electronic structure

ZnO TFT materials and homogenous QSL structures require metallization in devices. The interface with the metal is critical for low contact resistance, and for well-defined band bending. Within QSL structures, particular heterogeneous ones involving In, Ga and Zn oxides,<sup>40</sup> the interface between the QSL layers facilitated higher carrier mobility than each bulk material. Thus, the nature of the surface composition and electronic structure is important in homogeneous QSL structures.

To confirm the composition of the spin coated films and to assess the nature of O-vacancies that contribute to electronic conduction at the surface, XPS measurements were acquired of the Zn 2p, Zn 3p, and O 1s core-levels. All binding energies were corrected with reference to the C 1s photoelectric line centered at 284.8 eV. Figure 5(a) shows the Zn 2p core level spectra with the 2p spin-orbit doublet at binding energies of  $\sim 1022$  eV ( $2p_{3/2}$ ) and  $\sim 1045$  eV ( $2p_{1/2}$ ). The  $2p_{3/2}$  peak is nearly symmetric and represents photoemission from  $Zn^{2+}$  in ZnO.<sup>24</sup> The binding energy separation of the 2p doublet is consistently  $\sim 23$  eV. The O 1s spectrum for each ZnO thin film in Fig. 5(b) is asymmetric and comprised three separate contributions. The peaks are centered at  $\sim 533$ ,  $\sim 531.5$ , and  $\sim 530$  eV. The lowest energy photoemission,  $O_L$ , at 530 eV is assigned to the  $O^{2-}$  ions in the Zn–O lattice bonds and the central peak,  $V_O$ , at  $\sim 531.5$  eV is associated with  $O^{2-}$  ions near oxygen vacant regions.<sup>48</sup> Finally, the highest binding energy peak,  $O_H$ , is associated with chemisorbed oxygen in the form of hydroxyl groups.<sup>49</sup> The hydroxyl concentration, even after the annealing protocol in air, is very low and augers well for interfacing with dielectrics with low leakage currents.<sup>50</sup>

The resultant XPS spectra for an array of thin films of various thicknesses show a consistent binding energy and

intensity of the Zn 2p and O 1s peaks. The concentration of oxygen vacancies in solution-processed metal oxide semiconductors was previously related to calcination temperature.<sup>51,52</sup> The  $V_O$  to  $O_L$  ratio seen in Fig. 5(b) remains constant despite the cumulative variance in drying time for different QSL layer numbers. Since XPS is a surface sensitive measurement, probing a depth of  $<10$  nm into the sample surface, we propose that the surface consistency is due to all QSL samples receiving the same final annealing treatment ( $300^\circ\text{C}$  for 1 h), leaving a dense c-plane oriented ZnO outer surface in all cases. To examine the influence of the nature of the precursor on ZnO QSL thin films compositional and electronic quality, we also produced ZnO from acetate and oxide-based precursors, and corresponding XPS spectra can be seen in Fig. S2 in the supplementary material. The acetate precursor used in this work exhibits a lower density of  $V_O$  defects.

XPS data reveal an important finding for QSL electronic oxides such as ZnO grown this way, which may be worth considering in other homogeneous QSL materials (IZO, IGZO, and related). The surface chemistry and surface state are constant at the surface after drying and annealing, even when this total annealing time is cumulative so that c-plane orientation is possible throughout the film. With each additional periodic layer to the QSL, the top surface remains essentially identical, as a clean well-defined interface. A higher O vacancy content promotes n-type character as donors but also provides exceptional ambient air (moisture, O-containing air) stability for channel materials, as discussed by Liu *et al.*<sup>53</sup>

The surface electronic structure from Zn 2p and O 1s core-level photoemission is consistent and independent of QSL thickness. There is, however, a very slight shift in the binding energy of the Zn 2p spectra for a 1 L film. This is believed to be related to a marginal difference in the 1 L samples carrier concentration, discussed below. The valence

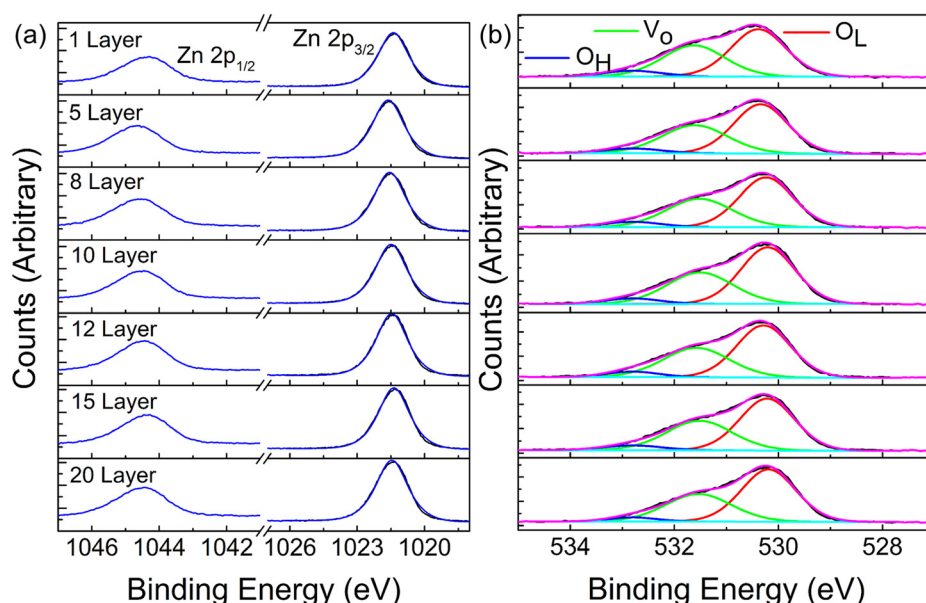


FIG. 5. (Color online) (a) X-ray photoelectron spectra from the hyperfine split Zn 2p core-level doublet from 1 L and 5–20 QSL thin film ZnO. (b) Corresponding O 1s core-level photoemission spectra.

band spectra shown in Fig. 6 confirm a shift of 0.77 eV between single and 20 QSL ZnO from  $-2.86$  eV for one layer to  $-2.11$  eV for 20 QSL. Using bandgap energies determined from optical transmission and PL characterization, and the valence band position relative to the Fermi level in Fig. 6(a), we constructed an effective band diagram for the ZnO QSL system in Fig. 6(b). The 1 L–20 QSL ZnO thin films exhibits a relatively consistent bandgap in the range 3.24–3.27 eV, but the valence band offset as a function of QSL thickness shifts the bands to lower energies (versus  $E_F$  or the vacuum energy), while  $E_g$  is relatively unchanged. Thus, 1 L ZnO exhibits a marginally higher effective n-type carrier concentration compared to 20 QSL ZnO. The data show the interesting behavior of homogeneous QSL structures. Optically, they behave as dispersive films of thickness equal to the QSL thickness, yet as QSL structures, the energy band diagram and overall electron affinity are affected by the number of layers in a well-ordered, compositionally identical material.

PL spectra of iteratively coated samples revealed a broad range of yellow-orange sub-bandgap defect emission [Figs. 7(a) and 7(b)]. Deep level emission in semiconducting metal oxide PL spectra are typically caused by defects in the crystal lattice, i.e., lattice interstitials and vacancies in the case of ZnO. This visible PL emission in undoped ZnO can be attributed to different intrinsic cationic and anionic interstitial and vacancy defects such as  $Zn_i$ ,  $O_i$ ,  $V_{Zn}$ ,  $V_O$ , and  $O_{Zn}$ .<sup>54</sup> The most recent work on ZnO PL has proposed Zn vacancies as the source of green emission, but examined using cathodoluminescence.<sup>55</sup> However, this explanation linked the vacancies to the m-plane of ZnO. Our QSL are predominantly c-axis oriented, and we propose the complexity arises from the structure of the ZnO nanocrystalline component within the less dense regions that can be probed by PL. UV photoexcitation of electrons to the CB is likely a contributory factor in the emission from defect states in comparison to x-ray probes, which cause photoemission of energetic electrons. Although not shown here, sub-band pumping of defect levels

shows no obvious defect emission; CB electrons required for PL emission for these ZnO QSL structures.

The obvious difference in the deep level emission between the different ZnO QSL PL spectra in Fig. 7(b) is in stark contrast to the uniformity of surface composition and electronic nature found by XPS for the same sample set in Fig. 5. In comparison to the XPS analysis, PL probes a greater depth, examining the bulk of the QSL structure and defects that contribute to radiative recombination. This PL analysis is sensitive to the porous material and the interfaces between it and the periodic dense layers, regions that the XPS technique is unable to probe. However, the PL emission signature is consistent across any region of an individual QSL structure.

The bandgap emission was observed at  $\sim 375$  nm (3.3 eV) in Fig. 7. Near band edge luminescence, caused by donor–acceptor pair (DAP) emission was also present and can cause widening of the bandgap peak. This is more obvious in some of the collected PL spectra, e.g., the 20 layer QSL sample in Fig. 7(a) shows a broad shoulder-peak on the bandgap emission at  $\sim 400$  nm. Bandgap blue-shift can also occur due to compressive strain on the crystal lattice. This is a factor for materials grown epitaxially on crystalline substrates whereas these ZnO thin films are deposited onto amorphous, thermally grown  $SiO_2$ . From Figs. 7(a) and 7(b), one layer ZnO shows negligible defect emission and in the main, both green and orange defect PL is noted in 20 QSL ZnO where considerable  $E_g$  and DAP emission is observed. Figure 7(c) summarizes the emission profile, and identifies orange PL as the most intense defect luminescence, but the defect band from QSL overall show green, orange or a combination once the number of layers and the recrystallization to c-axis orientation occurs. PL highlights the variety of electronic defects present contributing to the complex deep level emission as a function of the number of layers in the ZnO QSL.

Since the QSL has a particular nanocrystalline structure as part of each bilayer, and sub-band PL is rich with seemingly unique defect emission signatures, we then analyzed nine

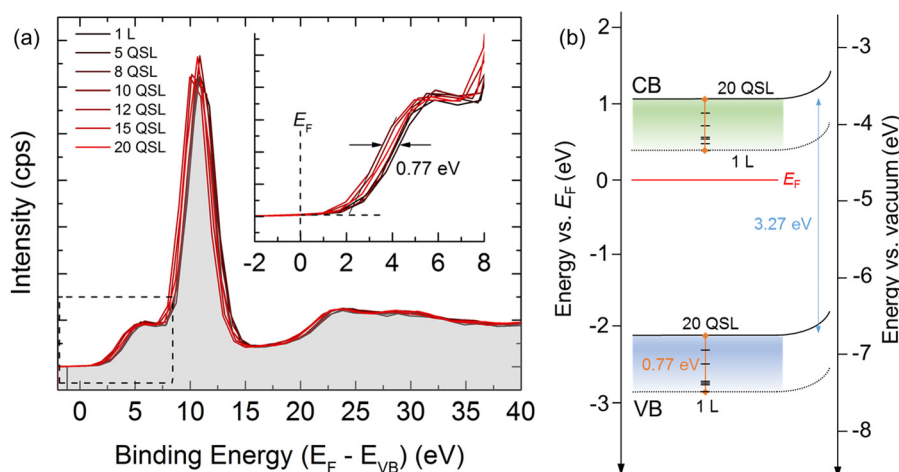


FIG. 6. (Color online) (a) Valence band spectra measured by XPS for 1 L–20 QSL ZnO thin films. (b) Energy band diagram for 1 L–20 QSL ZnO thin films constructed from XPS and band-edge absorption and photoluminescence data vs the Fermi energy ( $E_F$ ) and the vacuum energy scales. Highlighted CB and VB regions show the respective CB and VB shifts for 1 L to 20 QSL films, respectively.

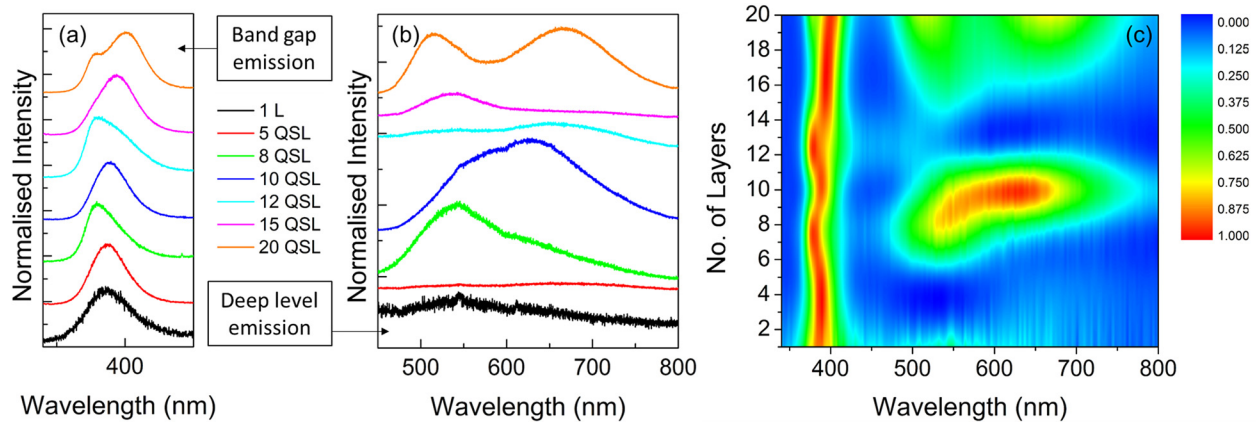


Fig. 7. (Color online) Photoluminescence spectra of ZnO separated into the (a) band edge and donor–acceptor pair emission, and (b) sub-band emission from radiative recombination via electronic defects within 1–20 QSL ZnO thin films. (c) Intensity color map showing the position of bandgap and defect level emission from ZnO films with increasing number of layers.

individual sites across the entire surface [Fig. 8(a)] of each sample in order to gauge the uniqueness but also the consistency of each PL response as a function of the number of layers. All individual spectra from nine regions from each of 1 L–20 QSL ZnO are provided in the supplementary material, Fig. S3. The spectra are remarkably consistent for each QSL thickness, with defined emission consistent across all regions of each deposited QSL. The PL intensity maps in Fig. 8(b)–8(h) show the nine collected PL spectra where the intensity of the bandgap emission and the deep level emission are easily comparable. The bandgap emission is consistently the highest intensity with exceptions in the 8 and 20 layers [Figs. 8(d) and 8(h)] where the deep level emission for some regions on the sample surface is more intense. Some regions on a particular sample did show hotspots of defect luminescence, but overall the unique PL signature from multilayered ZnO QSL are consistent across the full deposit. The five layer QSL

[Fig. 8(c)] shows consistent PL spectra with no shift in the bandgap emission and no obvious defect emission present. Notably, this five QSL materials also exhibited successively thinner iterative ZnO deposition, and maintains a dominant m-plane texture. For ZnO, as crystallinity improves, so does carrier mobility (for a single crystal). If crystallinity improvement also includes defect reduction, then consequently carrier concentration for n-type conduction would reduce. The difference between the PL mapping of the unique, but consistent, defect states of each QSL (compared to XPS data from surface chemical shifts), confirms qualitatively at least, that n-type conduction is largely unaffected by growth (deep donor defects such as  $V_O$  remain), and that conductivity is a function of the substructure and grain boundary resistance.

Defect emission in these ZnO thin films highlights how the internal electronic properties/defects are dependent on the cumulative layering of the films and the resultant change

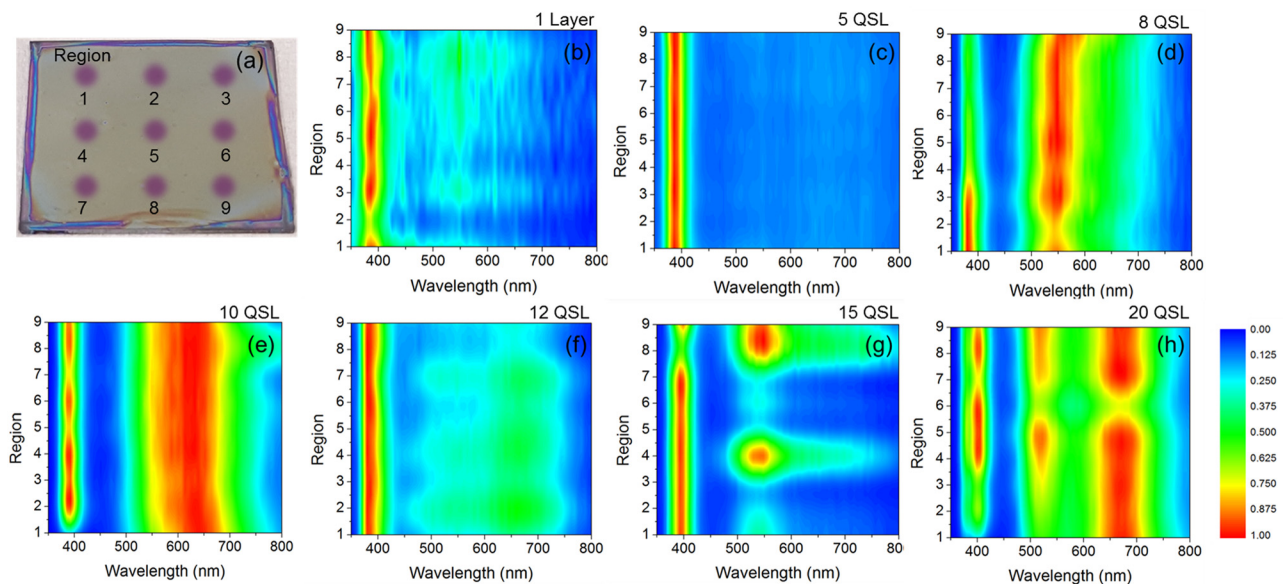


Fig. 8. (Color online) (a) Image of a ten layer ZnO thin film: colored regions represent areas at which PL spectra were collected for all samples. (b)–(h) Intensity color maps for 1, 5, 8, 10, 12, 15, and 20 layer QSLs, respectively, to show the PL spectra consistency obtained at nine regions across the sample surface.

in the heat energy supplied during deposition. The nature of the band edge and defect emission is consistent across the sample or deposit, and thus the emission is likely not related to randomly polycrystalline subsurface regions. The areal uniformity is from the dense upper most layer, which is chemically identical in all cases from XPS. PL emission is thus sensitive to interfaces between porous material and the dense layer in the QSL and serves as a fingerprint for each of the multilayered samples.

UV-vis optical transmittance and reflectance data for all QSL films are shown in Figs. 9(a) and 9(b). As we add layers to the QSL, we observe a clear and define onset of ZnO absorption in transmittance data, corresponding to the optical bandgap. This results in a red shift of the absorption edge compared to glass, in tandem with a reduction to 70% transmittance for one layer, to opacity for 20 layer QSL at  $E_g$ . Figure 9(b) shows the reflectance spectra of 1–20 layer ZnO thin films, collected at an angle of incidence of  $45^\circ$ . These spectra show that the deposited films are highly uniform and uniphase due to the characteristic sinusoidal interference patterns. Despite the film structure presenting as multilayers with homointerfaces, these reflectance spectra evidence that the films behave as continuous, coherent films. Due to this uniformity, a wavelength-dependent refractive index and the dispersive behavior of the QSLs, we have previously shown that it is possible to use an adapted method to calculate the optical thickness of the multilayered ZnO films (doped and undoped) which shows good agreement with physical thickness.<sup>44</sup>

From UV-vis transmittance measurements, we observe a suppression in transmittance from ZnO thin films at higher QSL number at wavelengths close to the bandgap ( $\sim 380$  nm), shown in Fig. 9(c). At longer wavelengths of 500 nm and

greater, the QSLs displays a consistent transmittance which coincides with the Tauc plot estimates. High transmittance at energies below the bandgap is consistent with oxygen deficient ZnO.<sup>56</sup> Using UV/vis transmittance data, the effective optical bandgap ( $E_g$ ) of ZnO thin films can be approximated using a Tauc plot for direct allowed transitions<sup>57</sup> and were calculated for all thin films and the glass substrate [Fig. 9(d)]. The bandgap for ZnO at room temperature is 3.37 eV.<sup>58</sup> For the ZnO QSLs grown on glass, there are two distinct linear regions from which  $E_g$  values can be extrapolated. Figure 9(d) shows that the higher energy value, observed for both the glass and 1 layer ZnO, demonstrates that  $\sim 40$  nm thick ZnO is transparent and sufficiently thin at normal incidence to cause significant increase in the absorbance with respect to the glass substrate, as can be seen in Fig. 9(a). For the 5–20 layer QSLs, we observe a short range in the optical transitions from 3.24 to 3.27 eV. We find that changes in overall optical transparency of the ZnO QSLs with increasing thickness/layer deposition in the visible are minimal.

#### IV. CONCLUSIONS

In this work, we have shown the growth and characterization of ZnO single-layer and QSL multilayered films via a solution-based spin-coating technique producing periodic multilayered films that are highly uniform and c-axis oriented. A near linear relationship between the thickness and number of deposited precursor layers is observed, explained by the decrease in the bilayer thickness with the increased number of depositions that forms the QSL structure. The surface of these films shows a smooth morphology with rms roughness  $< 0.14$  nm. Coherent multilayers of ZnO are shown to have epitaxial-like growth on an amorphous substrate with films displaying a change in the crystal growth direction from

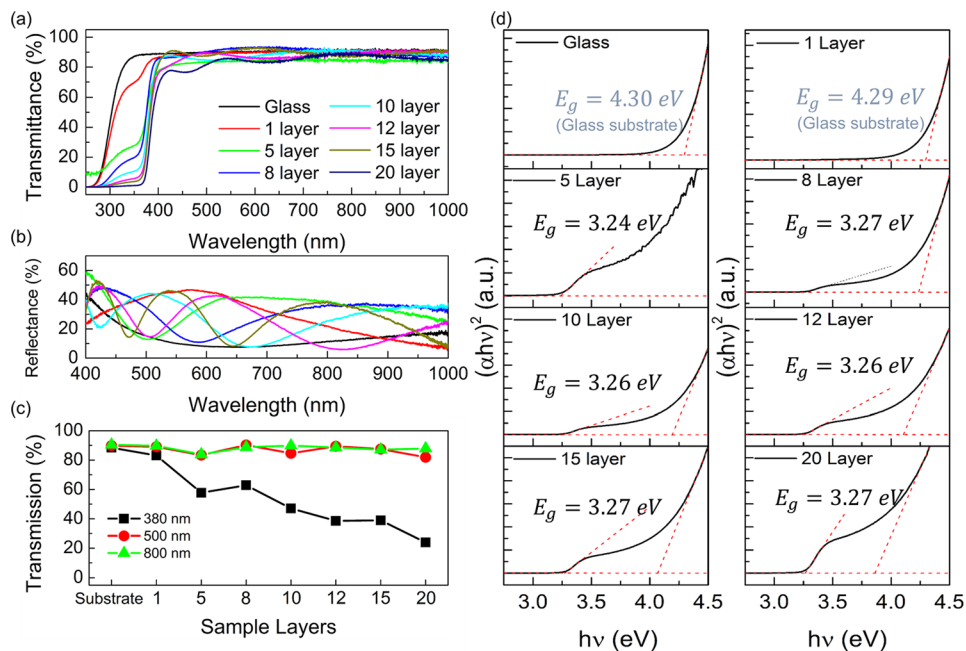


FIG. 9. (Color online) (a) UV/vis transmittance spectra for ZnO thin films deposited on glass substrates. (b) UV/vis reflectance spectra for 1 L–20 QSL acquired at  $\theta_i = 45^\circ$ . (c) Highlighting the percentage transmittance for ZnO QSLs at various wavelengths in the UV/vis. (d) Tauc plot analysis of ZnO QSLs to determine the optical bandgap. The value of  $E_g$  was calculated by extrapolating to  $[\hbar\omega]^2 = 0$  for both linear regions.

m-plane to c-plane homoepitaxy when the superlattice is grown. XPS confirmed a consistent composition and electronic structure of the terminating outer surface. PL emission from the ZnO QSL evidences a variety of electronic defects in the QSL bulk structure, specifically green and orange defect emission, that shows a marked dependence on the number of deposited layers and a sensitivity to the heating process applied during deposition. PL spectra across the deposited QSL surface show the unique emission profile is consistent for each QSL thickness. Our work presents an approach to accurately grow compositional homogeneous and periodically heterogeneous quasisuperlattice structure of ZnO, which has not been developed before. Our results shown that homogeneous ZnO structures, including mono, bi- and multilayered superlattice structures can be used to influence the spectral reflectance or transmittance, and electronic structure by altering the thickness, periodicity, crystalline orientation, and substructure of the oxide materials, while promoting homoepitaxy in a low temperature solution-based electronic material process.

## ACKNOWLEDGMENTS

D.B. acknowledges support of the Irish Research Council under Award No. GOIPG/2014/206. C.O. acknowledges support from the Science Foundation Ireland (SFI) through the SFI Technology Innovation and Development Award 2015 under Contract No. 15/TIDA/2893 and by a research grant from SFI under Grant No. 14/IA/2581.

- <sup>1</sup>K. Nomura, H. Ohta, A. Takagi, T. Kamiya, M. Hirano, and H. Hosono, *Nature* **432**, 488 (2004).
- <sup>2</sup>T. Kamiya, K. Nomura, and H. Hosono, *Sci. Technol. Adv. Mater.* **11**, 044305 (2010).
- <sup>3</sup>R. A. Street, *Adv. Mater.* **21**, 2007 (2009).
- <sup>4</sup>G. Huang, L. Duan, G. Dong, D. Zhang, and Y. Qiu, *ACS Appl. Mater. Interface* **6**, 20786 (2014).
- <sup>5</sup>C. Glynn and C. O'Dwyer, *Adv. Mater. Interfaces* **4**, 1600610 (2017).
- <sup>6</sup>H. Lingling *et al.*, *Jpn. J. Appl. Phys., Part 1* **54**, 04DJ07 (2015).
- <sup>7</sup>S. Shigehiko, H. Takeo, K. Motoki, K. Kazuto, Y. Mitsuaki, and I. Masataka, *Jpn. J. Appl. Phys., Part 1* **47**, 2845 (2008).
- <sup>8</sup>P. Yang *et al.*, *Adv. Funct. Mater.* **12**, 323 (2002).
- <sup>9</sup>M. H. Huang, S. Mao, H. Feick, H. Yan, Y. Wu, H. Kind, E. Weber, R. Russo, and P. Yang, *Science* **292**, 1897 (2001).
- <sup>10</sup>R. Könenkamp, R. C. Word, and C. Schlegel, *Appl. Phys. Lett.* **85**, 6004 (2004).
- <sup>11</sup>M.-C. Jeong, B.-Y. Oh, M.-H. Ham, and J.-M. Myoung, *Appl. Phys. Lett.* **88**, 202105 (2006).
- <sup>12</sup>X. Wang, C. J. Summers, and Z. L. Wang, *Nano Lett.* **4**, 423 (2004).
- <sup>13</sup>D. Calestani, M. Zha, R. Mosca, A. Zappettini, M. C. Carotta, V. Di Natale, and L. Zanotti, *Sens. Actuators, B* **144**, 472 (2010).
- <sup>14</sup>J. X. Wang, X. W. Sun, Y. Yang, H. Huang, Y. C. Lee, O. K. Tan, and L. Vayssieres, *Nanotechnology* **17**, 4995 (2006).
- <sup>15</sup>J. Jean, S. Chang, P. R. Brown, J. J. Cheng, P. H. Rekemeyer, M. G. Bawendi, S. Gradečak, and V. Bulović, *Adv. Mater.* **25**, 2790 (2013).
- <sup>16</sup>H. Park *et al.*, *Nano Lett.* **13**, 233 (2013).
- <sup>17</sup>Z. L. Wang and J. Song, *Science* **312**, 242 (2006).
- <sup>18</sup>Q. Zhang, C. S. Dandeneau, X. Zhou, and G. Cao, *Adv. Mater.* **21**, 4087 (2009).
- <sup>19</sup>Ü. Özgür, Y. I. Alivov, C. Liu, A. Teke, M. A. Reshchikov, S. Doğan, V. Avrutin, S.-J. Cho, and H. Morkoç, *J. Appl. Phys.* **98**, 041301 (2005).
- <sup>20</sup>E. Fortunato, P. Barquinha, and R. Martins, *Adv. Mater.* **24**, 2945 (2012).
- <sup>21</sup>R. Vázquez-Arreguín, M. Aguilar-Frutos, C. Falcony-Guajardo, A. Castañeda-Galván, L. Mariscal-Becerra, S. Gallardo-Hernández, G. Alarcón-Flores, and M. García-Rocha, *ECS J. Solid State Sci. Technol.* **5**, Q101 (2016).
- <sup>22</sup>F. K. Shan and Y. S. Yu, *J. Eur. Ceram. Soc.* **24**, 1869 (2004).
- <sup>23</sup>W. Taeg Lim and C. Hyo Lee, *Thin Solid Films* **353**, 12 (1999).
- <sup>24</sup>Y. Tak, D. Park, and K. Yong, *J. Vac. Sci. Technol., B* **24**, 2047 (2006).
- <sup>25</sup>L. Armelao, M. Fabrizio, S. Gialanella, and F. Zordan, *Thin Solid Films* **394**, 89 (2001).
- <sup>26</sup>Y. H. Hwang, J. H. Jeon, S.-J. Seo, and B.-S. Bae, *Electrochem. Solid-State Lett.* **12**, H336 (2009).
- <sup>27</sup>A. G. Emslie, F. T. Bonner, and L. G. Peck, *J. Appl. Phys.* **29**, 858 (1958).
- <sup>28</sup>C. Glynn, D. Creedon, H. Geaney, J. O'Connell, J. D. Holmes, and C. O'Dwyer, *ACS Appl. Mater. Interface* **6**, 2031 (2014).
- <sup>29</sup>K. Si Joon, Y. Seokhyun, and K. Hyun Jae, *Jpn. J. Appl. Phys., Part 1* **53**, 02BA02 (2014).
- <sup>30</sup>T. Schneller, R. Waser, M. Kosec, and D. Payne, *Chemical Solution Deposition of Functional Oxide Thin Films*, 1st ed. (Springer, London, 2013).
- <sup>31</sup>C. Glynn, D. Aureau, G. Collins, S. O'Hanlon, A. Etcheberry, and C. O'Dwyer, *Nanoscale* **7**, 20227 (2015).
- <sup>32</sup>S. Y. Park *et al.*, *Adv. Mater.* **24**, 834 (2012).
- <sup>33</sup>J. Chang, Z. Lin, M. Lin, C. Zhu, J. Zhang, and J. Wu, *J. Mater. Chem. C* **3**, 1787 (2015).
- <sup>34</sup>L.-C. Liu, J.-S. Chen, J.-S. Jeng, and W.-Y. Chen, *ECS J. Solid State Sci. Technol.* **2**, Q59 (2013).
- <sup>35</sup>H. Hosono, *J. Non-Cryst. Solids* **352**, 851 (2006).
- <sup>36</sup>K. K. Banger, Y. Yamashita, K. Mori, R. L. Peterson, T. Leedham, J. Rickard, and H. Sirringhaus, *Nat. Mater.* **10**, 45 (2011).
- <sup>37</sup>E. M. C. Fortunato, P. M. C. Barquinha, A. C. M. B. G. Pimentel, A. M. F. Gonçalves, A. J. S. Marques, L. M. N. Pereira, and R. F. P. Martins, *Adv. Mater.* **17**, 590 (2005).
- <sup>38</sup>H. Akazawa, *J. Vac. Sci. Technol., A* **35**, 021503 (2017).
- <sup>39</sup>J. G. Labram, N. D. Treat, Y.-H. Lin, C. H. Burgess, M. A. McLachlan, and T. D. Anthopoulos, *Adv. Funct. Mater.* **26**, 1656 (2016).
- <sup>40</sup>Y. H. Lin *et al.*, *Adv. Sci.* **2**, 1500058 (2015).
- <sup>41</sup>H.-A. Chin, I.-C. Cheng, C.-I. Huang, Y.-R. Wu, W.-S. Lu, W.-L. Lee, J. Z. Chen, K.-C. Chiu, and T.-S. Lin, *J. Appl. Phys.* **108**, 054503 (2010).
- <sup>42</sup>H. Faber *et al.*, *Sci. Adv.* **3**, e1602640 (2017).
- <sup>43</sup>J. G. Labram *et al.*, *Adv. Funct. Mater.* **25**, 1727 (2015).
- <sup>44</sup>D. Buckley, R. McCormack, and C. O'Dwyer, *J. Phys. D: App. Phys.* **50**, 16LT01 (2017).
- <sup>45</sup>B.-Z. Dong, G.-J. Fang, J.-F. Wang, W.-J. Guan, and X.-Z. Zhao, *J. Appl. Phys.* **101**, 033713 (2007).
- <sup>46</sup>T. Yamada, H. Makino, N. Yamamoto, and T. Yamamoto, *J. Appl. Phys.* **107**, 123534 (2010).
- <sup>47</sup>S. Hayamizu, H. Tabata, H. Tanaka, and T. Kawai, *J. Appl. Phys.* **80**, 787 (1996).
- <sup>48</sup>H.-B. Fan, S.-Y. Yang, P.-F. Zhang, H.-Y. Wei, X.-L. Liu, C.-M. Jiao, Q.-S. Zhu, Y.-H. Chen, and Z.-G. Wang, *Chin. Phys. Lett.* **24**, 2108 (2007).
- <sup>49</sup>M. N. Islam, T. B. Ghosh, K. L. Chopra, and H. N. Acharya, *Thin Solid Films* **280**, 20 (1996).
- <sup>50</sup>J. Hwang, K. Lee, Y. Jeong, Y. U. Lee, C. Pearson, M. C. Petty, and H. Kim, *Adv. Mater. Interface* **1**, 1400206 (2014).
- <sup>51</sup>Y.-H. Lin, H. Faber, K. Zhao, Q. Wang, A. Amassian, M. McLachlan, and T. D. Anthopoulos, *Adv. Mater.* **25**, 4340 (2013).
- <sup>52</sup>S. R. Thomas, P. Pattanasattayavong, and T. D. Anthopoulos, *Chem. Soc. Rev.* **42**, 6910 (2013).
- <sup>53</sup>L.-C. Liu, J.-S. Chen, and J.-S. Jeng, *ECS Solid State Lett.* **4**, Q59 (2015).
- <sup>54</sup>K. Vanheusden, W. L. Warren, C. H. Seager, D. R. Tallant, J. A. Voigt, and B. E. Gnade, *J. Appl. Phys.* **79**, 7983 (1996).
- <sup>55</sup>F. Fabbri *et al.*, *Sci. Rep.* **4**, 5158 (2014).
- <sup>56</sup>T. Minami, S. Ida, and T. Miyata, *Thin Solid Films* **416**, 92 (2002).
- <sup>57</sup>J. Tauc, *The Optical Properties of Solids* (Academic, New York, 1966).
- <sup>58</sup>J. Anderson and G. V. d. W. Chris, *Rep. Prog. Phys.* **72**, 126501 (2009).
- <sup>59</sup>See supplementary material at <http://dx.doi.org/10.1116/1.5001758> for AFM images of the ZnO QSL surfaces, XPS data of ZnO formed by acetate and oxide precursors and PL spectra from all regions of all ZnO QSL materials.